

Probing the extragalactic mid-infrared background with HAWC

A. ALBERT,¹ R. ALFARO,² C. ALVAREZ,³ J.C. ARTEAGA-VELÁZQUEZ,⁴ D. AVILA ROJAS,² H.A. AYALA SOLARES,⁵
 R. BABU,⁶ E. BELMONT-MORENO,² K.S. CABALLERO-MORA,³ T. CAPISTRÁN,⁷ A. CARRAMIÑANA,⁸ S. CASANOVA,⁹
 O. CHAPARRO-AMARO,¹⁰ U. COTTI,⁴ J. COTZOMI,¹¹ S. COUTIÑO DE LEÓN,¹² E. DE LA FUENTE,¹³ R. DIAZ HERNANDEZ,⁸
 M.A. DUVERNOIS,¹² M. DUROCHER,¹ J.C. DÍAZ-VÉLEZ,¹³ K. ENGEL,¹⁴ C. ESPINOZA,² K.L. FAN,¹⁴
 M. FERNÁNDEZ ALONSO,^{5,15} N. FRAIJA,⁷ J.A. GARCÍA-GONZÁLEZ,¹⁶ F. GARFIAS,⁷ M.M. GONZÁLEZ,⁷ J.A. GOODMAN,¹⁴
 J.P. HARDING,¹ S. HERNANDEZ,² D. HUANG,⁶ F. HUEYOTL-ZAHUANITLA,³ P. HÜNTEMAYER,⁶ A. IRIARTE,⁷
 A. JARDIN-BLICQ,^{17,18,19} V. JOSHI,²⁰ D. KIEDA,²¹ W.H. LEE,⁷ J.T. LINNEMANN,²² A.L. LONGINOTTI,⁷ G. LUIS-RAYA,²³
 K. MALONE,¹ O. MARTINEZ,¹¹ J. MARTÍNEZ-CASTRO,¹⁰ J.A. MATTHEWS,²⁴ P. MIRANDA-ROMAGNOLI,²⁵ E. MORENO,¹¹
 M. MOSTAFÁ,⁵ A. NAYERHODA,⁹ L. NELLEN,²⁶ M. NEWBOLD,²¹ M.U. NISA,²² R. NORIEGA-PAPAQUI,²⁵ N. OMODEI,²⁷
 A. PEISKER,²² Y. PÉREZ ARAUJO,⁷ E.G. PÉREZ-PÉREZ,²³ C.D. RHO,²⁸ D. ROSA-GONZÁLEZ,⁸ H. SALAZAR,¹¹
 D. SALAZAR-GALLEGOS,²² F. SALESA GREUS,^{9,29} A. SANDOVAL,² J. SERNA-FRANCO,² A.J. SMITH,¹⁴ Y. SON,²⁸
 R.W. SPRINGER,²¹ O. TIBOLLA,²³ K. TOLLEFSON,²² I. TORRES,⁸ R. TORRES-ESCOBEDO,³⁰ R. TURNER,⁶ F. UREÑA-MENA,⁸
 L. VILLASEÑOR,¹¹ X. WANG,⁶ T. WEISGARBER,¹² E. WILLOX,¹⁴ AND H. ZHOU⁴
 et al.

HAWC COLLABORATION

¹Physics Division, Los Alamos National Laboratory, Los Alamos, NM, USA²Instituto de Física, Universidad Nacional Autónoma de México, Ciudad de Mexico, Mexico³Universidad Autónoma de Chiapas, Tuxtla Gutiérrez, Chiapas, México⁴Universidad Michoacana de San Nicolás de Hidalgo, Morelia, Mexico⁵Department of Physics, Pennsylvania State University, University Park, PA, USA⁶Department of Physics, Michigan Technological University, Houghton, MI, USA⁷Instituto de Astronomía, Universidad Nacional Autónoma de México, Ciudad de Mexico, Mexico⁸Instituto Nacional de Astrofísica, Óptica y Electrónica, Puebla, Mexico⁹Institute of Nuclear Physics Polish Academy of Sciences, PL-31342 IFJ-PAN, Krakow, Poland¹⁰Centro de Investigación en Computación, Instituto Politécnico Nacional, México City, México.¹¹Facultad de Ciencias Físico Matemáticas, Benemérita Universidad Autónoma de Puebla, Puebla, Mexico¹²Department of Physics, University of Wisconsin-Madison, Madison, WI, USA¹³Departamento de Física, Centro Universitario de Ciencias Exactas e Ingenierías, Universidad de Guadalajara, Guadalajara, Mexico¹⁴Department of Physics, University of Maryland, College Park, MD, USA¹⁵Gran Sasso Science Institute (GSSI), Via Iacobucci 2, I-67100 L'Aquila, Italy¹⁶Tecnologico de Monterrey, Escuela de Ingeniería y Ciencias, Ave. Eugenio Garza Sada 2501, Monterrey, N.L., Mexico, 64849¹⁷Max-Planck Institute for Nuclear Physics, 69117 Heidelberg, Germany¹⁸Department of Physics, Faculty of Science, Chulalongkorn University, 254 Phayathai Road, Pathumwan, Bangkok 10330, Thailand¹⁹National Astronomical Research Institute of Thailand (Public Organization), Don Kaeo, MaeRim, Chiang Mai 50180, Thailand²⁰Erlangen Centre for Astroparticle Physics, Friedrich-Alexander-Universität Erlangen-Nürnberg, Erlangen, Germany²¹Department of Physics and Astronomy, University of Utah, Salt Lake City, UT, USA²²Department of Physics and Astronomy, Michigan State University, East Lansing, MI, USA²³Universidad Politécnica de Pachuca, Pachuca, Hgo, Mexico²⁴Dept of Physics and Astronomy, University of New Mexico, Albuquerque, NM, USA²⁵Universidad Autónoma del Estado de Hidalgo, Pachuca, Mexico²⁶Instituto de Ciencias Nucleares, Universidad Nacional Autónoma de México, Ciudad de Mexico, Mexico²⁷Department of Physics, Stanford University: Stanford, CA 94305-4060, USA²⁸University of Seoul, Seoul, Rep. of Korea²⁹Instituto de Física Corpuscular, CSIC, Universitat de València, E-46980, Paterna, Valencia, Spain³⁰Tsung Dao Lee Institute and School of Physics and Astronomy, Shanghai Jiao Tong University, Shanghai, China

Corresponding author: M. Fernández Alonso

mkf5479@psu.edu

ABSTRACT

The extragalactic background light (EBL) contains all the radiation emitted by nuclear and accretion processes in stars and compact objects since the epoch of recombination. Measuring the EBL density directly is challenging, especially in the near- to far-infrared waveband, mainly due to the zodiacal light foreground. Instead, gamma-ray astronomy offers the possibility to indirectly set limits on the EBL by studying the effects of gamma-ray absorption in the very high energy (VHE: >100 GeV) spectra of distant blazars. The High Altitude Water Cherenkov gamma ray observatory (HAWC) is one of the few instruments sensitive to gamma rays with energies above 10 TeV. This offers the opportunity to probe the EBL in the near/mid IR region: $\lambda = 1 \mu\text{m} - 100 \mu\text{m}$. In this study, we fit physically motivated emission models to *Fermi Large Area Telescope (LAT)* GeV data to extrapolate the intrinsic TeV spectra of blazars. We then simulate a large number of absorbed spectra for different randomly generated EBL model shapes and calculate Bayesian credible bands in the EBL intensity space by comparing and testing the agreement between the absorbed spectra and HAWC extragalactic observations of two blazars. The resulting bands are in agreement with current EBL lower and upper limits, showing a downward trend towards higher wavelength values $\lambda > 10 \mu\text{m}$ also observed in previous measurements.

1. INTRODUCTION

The extragalactic background light (EBL) comprises all radiation released by nuclear and accretion processes since the epoch of recombination. It consists of all emitted radiation from stars and compact object surroundings, including that absorbed/re-emitted by dust and accumulated over all redshifts. Measuring and constraining this background radiation is crucial to understand star formation processes and galaxy evolution models. Our current knowledge of the EBL is limited, its direct measurements are challenging due to foreground contamination coming, mainly, from the zodiacal light. However, upper and lower limits have been established using various methods, e.g. integrated galaxy counts from optical observations with the Hubble Space Telescope (Gardner et al. 2000; Madau & Pozzetti 2000) and infrared (IR) observations using the Spitzer Space Telescope (Fazio et al. 2004; Papovich et al. 2004) and the Infrared Space Observatory (Elbaz et al. 2002). An extensive discussion on EBL related matters can be found in Elbaz et al. (2002), Orr et al. (2011) and Cooray (2016).

Over the past two decades, VHE gamma-ray observations have been used to help constrain the spectral properties of the EBL, particularly with observations from blazars, a sub-type of Active Galactic Nuclei (AGN) with ultra-relativistic jets oriented close to the observer’s line of sight. VHE gamma rays coming from blazars interact via pair production with the EBL photons (Gerasimova et al. 1962; Gould & Schröder 1967) producing imprints in the observed energy spectra of distant sources. These imprints, along with intrinsic spectral assumptions, can be used to derive limits on the EBL **near/mid IR range using VHE observations of blazars** (e.g. Aharonian et al. 2007; Mazin &

Raue 2007; Orr et al. 2011; Biteau & Williams 2015; Abdalla et al. 2017; Abeysekara & Archer 2019; Acciari & Ansoldi 2019). The gamma-ray horizon establishes the energy at which the intensity of radiation is diminished by a factor $1/e$ with respect to the emitted intensity. This energy value depends on the distance of the source and it needs to be taken into account when selecting suitable candidate sources for this type of study. If the source is too close, the absorption effect will only be measurable at higher energies, where, depending on the detector and the energy of the gamma ray, the sensitivity might be too low. On the other hand, distant sources will be dimmer, precisely due to the EBL absorption, so these are not ideal candidates to work with either (Franceschini et al. 2019). Equation 1 approximately relates the energy of a gamma ray (E_γ) with the wavelength range of the EBL radiation (λ_{EBL}) involved in the pair production interaction:

$$\lambda_{EBL} \sim [0.5 \mu\text{m} - 5 \mu\text{m}] \times \left(\frac{E_\gamma}{1 \text{ TeV}} \right) \times (1+z)^2. \quad (1)$$

where z is the redshift of the source emitting the gamma ray. This equation is useful to estimate the EBL probing power when considering a specific source observed with a specific instrument.

The High Altitude Water Cherenkov gamma ray observatory (HAWC) is a water Cherenkov detector that has been operational since 2015 (further technical details can be found in section 2), and that has detected extragalactic sources significantly up to 10 TeV (Albert et al. 2021a). This energy is close to the one established by the gamma-ray horizon for sources like the two blazars Markarian 501 and Markarian 421 (from now on referred to as *Markarians*), putting HAWC in an advantageous

position to potentially probe the mid-IR region of the EBL using observations from these sources.

In this study, physically motivated emission models and data from the *Fermi Large Area Telescope* (*Fermi-LAT*) are used to construct an intrinsic spectrum for each of the Markarians (see section 3.1). A large number of randomly generated EBL model shapes are used to apply the EBL attenuation effect to these intrinsic spectra to compare with HAWC data (see section 3.2). The comparison is performed using *threeML*¹, a software package for likelihood fitting, in a way that each EBL model can be assigned a likelihood value that expresses the agreement between that particular spectral realization and HAWC data (see section 3.3). This method has the advantage of being independent of any particular EBL shape and of assuming physically motivated intrinsic spectral properties for the sources. Finally, weights are applied to each model in accordance to their calculated likelihood value, and credible intervals in the EBL spectral energy distribution (SED) space are derived (section 4).

2. DATA: HAWC & *FERMI-LAT*

HAWC is an array of 300 water Cherenkov detector tanks located in Sierra Negra, Mexico, at an altitude of 4100 m above the sea level and covering a total area of 22000 m². Each tank has four photo-multiplier tubes (PMTs) facing upwards that can detect the Cherenkov light in the water from the transit of secondary particles, which are produced by gamma rays and cosmic rays interacting with the atmosphere. HAWC triggers with a rate of 25 kHz and has a duty cycle of >95%. The observatory continuously monitors 2/3 of the sky, detecting gamma rays in the energy range between 100 GeV and several hundred TeV. More information on the HAWC observatory operation, performance and the way air shower event data are reconstructed can be found in Abeysekara & Albert (2017). For this analysis, specific *Fermi-LAT* and HAWC data from the blazars Markarian 421 ($z = 0.031$) and Markarian 501 ($z = 0.034$) were selected (redshift sourced from NED²). These are two extensively studied extragalactic sources and the brightest in the TeV band. Both sources have been significantly detected by HAWC above 300 GeV up to 10 TeV (Albert et al. 2021a) and by *Fermi-LAT* between 100 MeV and 1 TeV (Abdo et al. 2011; Abdo & Ack-

ermann 2011). For the HAWC dataset, 1343 days of data were used, taken between **June 2015 and June 2019** (Abeysekara et al. 2019). The analysis was performed using maps created with a special algorithm for reconstructing and determining the energy of the primary gamma rays. This algorithm, denominated ground parameter algorithm, is based primarily on the charge density at a fixed optimal distance from the shower axis and it divides the energy range into quarter-decade bins in $\log_{10}(E)$, beginning at $\log(E/\text{TeV})=-0.5$ (0.316 TeV) and ending at $\log(E/\text{TeV})=2.5$ (316 TeV). The ground parameter energy estimator was chosen because it is optimal for higher energies, between 10 TeV and 316 TeV (Abeysekara et al. 2019), where the instrument could potentially probe the EBL mid-IR region. For the *Fermi-LAT* dataset, a time period corresponding to the HAWC dataset was selected between 57180 - 58640 MJD. This dataset is within the energy range of 100 MeV - 316 GeV, where the absorption is, at most, around 5% for the Markarians redshift³. The *Fermi-LAT* analysis is described in more detail in section 3.1.

3. EBL ANALYSIS

The approach adopted in this study consists of calculating EBL intensity limits by comparing the expected absorbed flux with actual HAWC observations. The method is similar to previous EBL studies: Mazin & Raue (2007), Orr et al. (2011), Biteau & Williams (2015) and, in particular, to Abeysekara & Archer (2019), presented by the VERITAS collaboration. In the latter analysis, a large number of random generated EBL models is used to calculate the corresponding de-absorbed spectra of selected blazars, and then each model is weighted using criteria based on intrinsic assumptions for these sources to finally derive limits to the EBL intensity. In the present analysis, the EBL models are used to simulate the absorption effect which is then applied over the assumed intrinsic spectra. The resulting absorbed spectra are then compared to the real HAWC data by calculating a likelihood value. Finally, each EBL model is weighted according to their corresponding likelihood value.

3.1. Intrinsic Spectra: *Fermi-LAT* & *Naima*

A possible and reasonable assumption is to consider the intrinsic TeV spectrum of a given source as an extension of a physical emission model that is in agreement with GeV observations. This assumption relies on the fact that gamma rays in the high energy regime (HE: 100 MeV - 100 GeV) and relatively low redshifts

¹ <https://threeml.readthedocs.io/en/stable/index.html>

² The NASA/IPAC Extragalactic Database (NED) is operated by the Jet Propulsion Laboratory, California Institute of Technology, under contract with the National Aeronautics and Space Administration.

³ estimated assuming the Domínguez et al. (2011a) EBL model

($z \lesssim 0.1$) are not significantly affected by EBL absorption, and therefore the observed spectrum can be safely considered to be practically the same as the intrinsic one (e.g. Abdo et al. 2010; Orr et al. 2011; Furniss et al. 2013). In the present study, a *Fermi-LAT* standard fitting analysis was performed to obtain spectral flux points corresponding to Markarian 421 and Markarian 501, using observations from a similar time period as the one observed by HAWC (for details see section 2). The *Fermi-LAT* analysis was carried out using the instrument response function P8R2_SOURCE_V6, and the spectral parameters are estimated by the binned maximum likelihood method using the *Fermipy v.0.17.3* package. The analysis was also performed with a zenith cut of 90° and, as mentioned in section 2, within the energy range of 100 MeV - 316 GeV to minimize possible absorption effects while including as much data as possible. The events were extracted within a 10 degree region of interest (RoI) centered on each source position. The background model includes sources from the Preliminary *Fermi-LAT* 8-year point sources catalog⁴, Galactic diffuse emission *glliemv06.fits* and the isotropic diffuse emission *isoP8R2SOURCEV6v06.txt* models.

To avoid the overestimation of the intrinsic flux, each source lowest energy fluxpoint observed by HAWC (Albert et al. 2021a) is used as a guide; observed Mrk 421 and Mrk 501 fluxpoints at an energy of 830 GeV and 750 GeV, respectively, are de-absorbed according to Franceschini et al. (2008) model. These de-absorbed fluxpoints are included in the set of flux points obtained from the *Fermi-LAT* analysis described above, and altogether are used to fit a physically motivated emission model with *Naima*, a Python software software that calculates the non-thermal emission from a leptonic or hadronic population of particles (Zabalza 2015).

In this case, the dataset is fit with a Synchrotron-Self-Compton (SSC) model, a scenario in which synchrotron radiation is produced by electrons moving at relativistic velocities in randomly oriented magnetic fields and up-scattered by inverse Compton into higher energies by the same electron population. The leptonic distribution is chosen to follow an exponentially cut-off powerlaw (ECPL) distribution:

$$f(E) = A \left(\frac{E}{E_0} \right)^{-\alpha} \exp \left(-\frac{E}{E_c} \right). \quad (2)$$

where A is a normalization factor, E_0 is a reference energy set at 1 TeV, α is the power law index and E_c the cut-off energy. The decision for this particular leptonic

distribution is motivated by other studies performed on the Markarians by HAWC (Albert et al. 2021a) and others (Zhu et al. 2016; Abdo & Ackermann 2011). Based on the results reported in Albert et al. (2021a), **the magnetic field and emission radius values are set at 0.03 G and 4×10^{16} cm for Mrk 421 and 0.02 G and 1×10^{17} cm for Mrk 501, respectively.** Table 1 shows the best fit parameters for the electron distributions of each source. The best fit models are then extrapolated into TeV energies (see figure 2) and used as templates for the intrinsic spectra of the sources (see section 3.3).

3.2. EBL models

To generate different EBL model shapes, a grid of 12 λ -values across the wavelength of the EBL photons between $1 \mu\text{m}$ and $100 \mu\text{m}$ is set. For each λ -value, **an intensity ($\text{nW m}^{-2} \text{sr}^{-1}$) value is assigned by randomly generating a number between $1 \text{ nW m}^{-2} \text{sr}^{-1}$ and $50 \text{ nW m}^{-2} \text{sr}^{-1}$, resulting in a flat initial distribution in EBL intensity;** the range is chosen to contain the EBL upper and lower limits discussed in section 1. A particular EBL shape is defined by interpolating each intensity point corresponding to each wavelength, using second order splines. To avoid sharp model shapes, intensity at consecutive grid points is not allowed to change by more than a factor of 2. For this reason and, since the interpolation is performed in increasing order in λ , intensities for higher λ values are more conditionally sampled than lower λ values. This bias, is then corrected by weighting the intensities in each grid point to recover the initial flat intensity distribution. Avoiding sharp models that are nonphysical has the caveat of neglecting possible features coming from polycyclic aromatic hydrocarbons, known to be present in the mid-IR range (Lagache et al. 2005). However, for relatively small redshifts, like those considered in this analysis, these sharp features would be smoothed out to a bump (Domínguez et al. 2011b). Figure 1 shows examples of EBL shapes generated in this way. A total of 30000 models are generated at redshift $z = 0$. The EBL intensity can be then used to compute the optical depth $\tau(E, z)$, which quantifies the absorption effect of gamma rays with energy (E) and traveling a given distance associated with a redshift value z . The theoretical framework behind these calculations can be found in e.g. Dwek & Krennrich (2013); Biteau & Williams (2015); Abdalla et al. (2017). In this analysis, the τ values are computed using the *ebtable* Python package⁵

⁴ <https://fermi.gsfc.nasa.gov/ssc/data/access/lat/f8y/>

⁵ <https://github.com/me-manu/ebtable>

Table 1. Electron distribution parameters resulting from the SSC emission model likelihood fit performed with NAIMA to *Fermi-LAT* data from Mrk 421 and Mrk 501. A is a normalization factor, E_0 is a reference energy set at 1 TeV, α is the power law index and E_c the cut-off energy

| Parameter | Mrk 421 | Mrk 501 |
|-------------|--------------------------------|--------------------------------|
| α | 2.77 ± 0.02 | 2.75 ± 0.04 |
| E_c [TeV] | $(1.2 \pm 0.9) \times 10^1$ | $(1.85 \pm 0.75) \times 10^1$ |
| A [1/eV] | $(1.4 \pm 0.1) \times 10^{36}$ | $(0.9 \pm 0.1) \times 10^{36}$ |

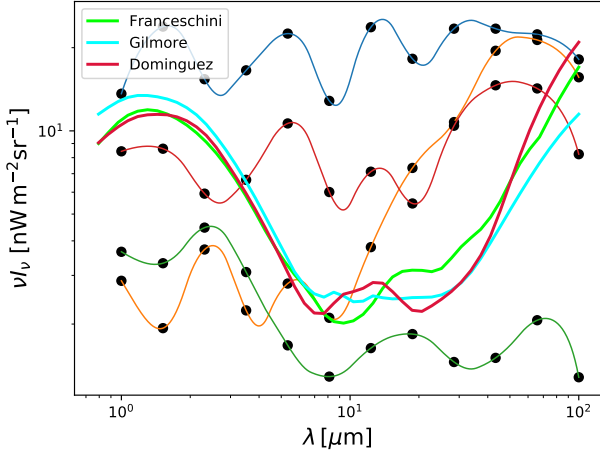


Figure 1. Sample of spline-interpolated models in the EBL spectral density space. Also shown, Franceschini et al. (2008), Domínguez et al. (2011b) and Gilmore et al. (2012) EBL models shapes.

to read in and interpolate tables for EBL density and to calculate the resulting opacity for high energy gamma rays. The τ values are computed between 0.1 and 50 TeV and for redshifts between 0.03-0.04, chosen respectively to include the Markarian’s highest energy points measured by HAWC and their redshift. The points at which the calculations are done are evenly spaced in logarithmic space in energy, and linearly in redshift. A flat Λ CDM cosmology is assumed in the calculation, with dark-energy density $\Omega_\Lambda = 0.73$, matter density $\Omega_M = 0.27$, and Hubble constant $H_0 = 70 \text{ km s}^{-1} \text{ Mpc}^{-1}$. The EBL number density η_{EBL} is scaled with redshift as $(1+z)^{3-f_{\text{evo}}}$ (Madau & Phinney 1996), and a value of $f_{\text{evo}} = 1.7$ (evolution factor) is chosen following Abeysekara & Archer (2019), where they find it to be consistent with the Franceschini et al. (2008), Domínguez et al. (2011b) and Gilmore et al. (2012) EBL models. The calculated opacity for each redshift-energy is then used to simulate the absorption process by applying the attenuation factor to the assumed intrinsic differential flux in the following way:

$$\frac{dN}{dE_{\text{obs}}} = \frac{dN}{dE_{\text{int}}} \times e^{-\tau(E,z)}. \quad (3)$$

where $\frac{dN}{dE_{\text{obs}}}$ is the observed differential flux and $\frac{dN}{dE_{\text{int}}}$ the assumed intrinsic differential flux.

Figure 2 shows Mrk 421 *Fermi-LAT* flux points with its corresponding *Naima-SSC* fit extrapolated into TeV energies. An example of the absorbed spectrum according to an EBL model along with HAWC data is also shown.

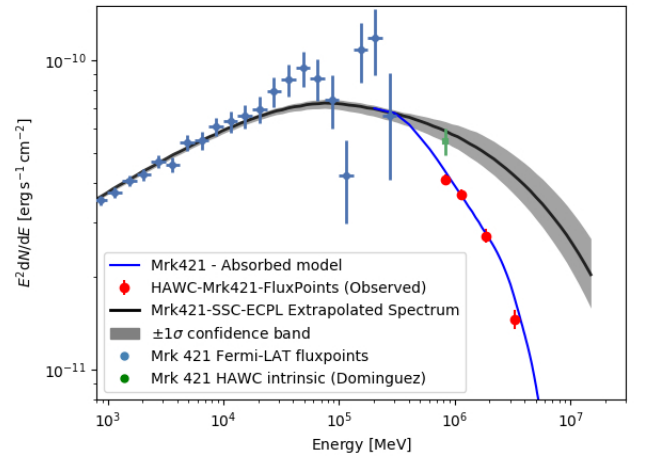


Figure 2. Extrapolated intrinsic emission spectrum for Mrk 421 (black line) along with the $\pm 1\sigma$ confidence band (statistical uncertainty only). Also shown, the resulting absorbed spectrum (blue line) according to a random EBL model along with HAWC data, the fluxpoints resulting from the *Fermi-LAT* analysis (light-blue points) and the de-absorbed HAWC fluxpoint (green) according to Franceschini et al. (2008) EBL model.

3.3. *threeML* framework, likelihood and limit extraction

The comparison between the expected absorbed model and HAWC data, is performed adopting a Bayesian approach and using the Multi-Mission Maximum Likelihood framework (Vianello et al. 2015; Younk et al. 2015). This analysis pipeline is capable of handling data from a wide variety of astrophysical detectors. In this particular study the HAWC plugin (HAL⁶) is used.

⁶ https://github.com/threeML/hawc_hal

The HAL fitting technique is based on a forward-folding method that assumes a spectral model shape for the source. In this case, a SSC source emission model is built using the *astromodels* package, a useful framework to define models for likelihood or Bayesian analysis of astrophysical data⁷. This emission model is customized for each source by plugging in the fit parameters obtained from the *Naima* fit described in section 3.1, to create an intrinsic spectrum that serves as an input for the threeML fitting pipeline. The EBL absorption is applied to the emission model while their spectral parameters are kept fixed. Finally, the forward-folding method, including detector response effects, is performed to fit the absorbed spectrum of the source using a maximum likelihood technique (Younk et al. 2015) to calculate a likelihood value for the fit (\mathcal{L}). The process is repeated for each of the 30000 EBL models generated as explained in section 3.2. In this way, instead of optimizing the parameters of the source to find the ones that give the maximum likelihood, these are kept fixed, and only the EBL models are evaluated by their ability to reproduce the data. After the test, each EBL model is assigned a likelihood value that quantifies the agreement between that particular *emission + absorption* model and the actual data. The maximum likelihood value corresponds to the EBL model whose simulated absorption best reproduces HAWC observations. Starting off from a prior flat intensity distribution for each wavelength, resulting from the uniform sampling described in section 3.2, each model intensity is then assigned a weight as follows:

$$W_i = \frac{\mathcal{L}_i}{\mathcal{L}_{max}}. \quad (4)$$

where \mathcal{L}_i is the likelihood value corresponding to the “i-th” EBL model. The intensities corresponding to the *maximum-likelihood* model are then assigned a weight of 1 and the rest of the model intensities are weighted by a factor of $\mathcal{L}_i/\mathcal{L}_{max}$, disfavoring EBL shapes that differ from the EBL model that best agrees with data. This approach is based on the idea of *relative likelihood*, which is an estimate of the probability of a model to reproduce data, normalized by the maximum likelihood value (Kalbfleisch 1985). When combining results from both sources, each EBL model is weighted by multiplying the individual source weights previously calculated: $W_{mrk421} \times W_{mrk501}$. For each λ -value, the *maximum-likelihood* EBL models from each source are used to calculate an average intensity value for the combined result.

A projection of the EBL intensity probability for each value of λ can be obtained from the histogram

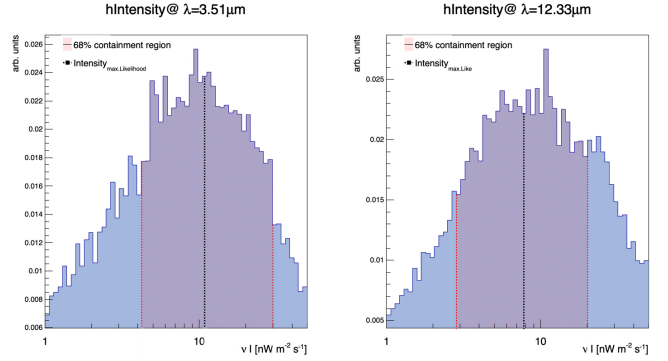


Figure 3. Weighted intensity distributions for $\lambda = 3.5\mu\text{m}$ and $\lambda = 12.3\mu\text{m}$. The red hatching corresponds to the 68% containment region. Black dashed line represents the intensity corresponding to the maximum likelihood model at that particular value of λ .

of weighted intensities, which represents the posterior distribution of intensities at that λ given the observed data. Figure 3 shows an example of these distributions for two values of λ . The distributions are initially (pre-weighting) flat on average, but fluctuate in accordance with the random sampling described in section 3.2. This explains why the intensity corresponding to the *maximum-likelihood* model (black-dashed line in figure 3), in spite of having the greatest weight, does not necessarily correspond with the maximum of the distribution.

The credible intervals (analogous to confidence intervals in frequentist statistics) are obtained by integrating the 0.68 and 0.95 containment regions from the λ value corresponding to the *maximum-likelihood* model outwards. In this way, the 68% and 95% containment regions are defined around the model which best reproduces the data. For some wavelength values, the corresponding distributions are such that the limits fall outside considered range of intensity. For these cases, the containment region is reported without a lower/upper boundary. To test the sensitivity of the method to the prior assumptions, the procedure is repeated varying the smoothing condition between consecutive knots and alternatively sampling a flat distribution in logarithm of the intensities instead of the original linear sampling (see section 3.2). No significant changes are observed throughout the process with respect to the original prior conditions.

4. RESULTS AND DISCUSSION

The containment regions are calculated assuming SSC emission models from ECPL-leptonic distributions for both Mrk 421 and Mrk 501 intrinsic spectral models, as explained in section 3.1. Figure 4 shows the resulting

⁷ <https://astromodels.readthedocs.io/en/latest/>

68% and 95% containment regions for each of the considered sources as a function of wavelength. The intensities corresponding to the model with the highest likelihood are shown in black circles, along with lower limits from galaxy counts and upper limits from direct measurements shown as upward and downward triangles, respectively.

Figure 5 shows the resulting 68% and 95% containment regions when combining the results from both sources. The combined intensities from each source's highest likelihood model are shown in black circles along with results from other experiments (Abeysekara & Archer 2019; Acciari & Ansoldi 2019; Abdalla et al. 2017). Everything else in the plot is identical to what is shown in figure 4. From figure 5 it is clear that for some λ -values, namely $30\mu\text{m} < \lambda$ for Mrk 421 and $\lambda < 4\mu\text{m} \cup 10\mu\text{m} < \lambda$ for Mrk 501, boundaries cannot be established (see section 3.3), limits in these cases are not reported (these are shown as a dash in table 2).

The containment bands are in good agreement with the region delimited between the lower and upper limits from galaxy counts and direct measurements respectively. However, for wavelengths lower than $\lambda \sim 5\mu\text{m}$, the containment region is broader than the limits, so results are non-constraining in this range. Combined results show a general downward tendency in the EBL measurement for λ values $> 5\mu\text{m}$, following the lower limits from galaxy counts. This downward trend has been observed also by VERITAS (Abeysekara & Archer 2019) and MAGIC (Acciari & Ansoldi 2019). In the case of HAWC, this could be explained by the fact that the highest observed data points (> 7 TeV), especially for Mrk 501, show an upward trend (see Albert et al. (2021a)), leading to lower EBL density values for this wavelength range. HAWC observed spectrum of Mrk 421 shows a cutoff energy around 5 TeV, this could, in principle, be related to the bump around $20\mu\text{m}$ seen in Mrk 421 results (see figure 4).

4.1. Systematic uncertainties

There are many sources of systematic uncertainties that affect the flux estimation from HAWC observations, mostly coming from discrepancies between data and simulations, arising from mis-modeling of the detector. A complete treatment of HAWC possible systematics is presented in Abeysekara et al. (2019), in which they found that the dominant systematic uncertainties for the spectral flux come from mis-modeling the late light in the air shower and the uncertainty in the modeling of the PMT efficiencies and the charge measured by the PMTs. To estimate the potential effect of these systematics in the overall results, the analysis is repeated

simulating extreme detector responses considering these dominant systematics. Results in each case are compared with nominal results. Figure 6 shows the relative difference for each wavelength between each considered systematic and the nominal results quantified in the following manner:

$$\Delta = \frac{\nu I_{\nu}^{nom} - \nu I_{\nu}^{sys}}{\sqrt{\sigma_{nom}^2 + \sigma_{sys}^2}}. \quad (5)$$

where I_{ν}^{nom} and I_{ν}^{sys} are the EBL density values, at each wavelength, resulting from the nominal model and the considered extreme systematic model respectively; σ_{nom}^2 and σ_{sys}^2 are the corresponding errors, at each wavelength, for the nominal and systematic results respectively.

No significant ($\Delta > 3$) difference is observed between the results from the nominal model and those coming when considering extreme systematics. It is important to note that the fact systematics are not significant is, in this case, mostly due to the relatively large errors associated with the method, rather than the instrumental uncertainty being small.

4.2. Intrinsic model uncertainties

The selection for a particular emission model, magnetic field and emission radius (see section 3.1) introduces a bias that will eventually impact the calculated EBL limits. As mentioned in section 3.1, the choice on the parameter values and model is based on previous studies performed on the markarians (Albert et al. 2021a; Zhu et al. 2016; Abdo & Ackermann 2011). However, Two additional models following the contours of the $\pm 1\sigma$ confidence band (see figure 2) given by the fit described in section 3.1, are also considered. These models are used to repeat the analysis in order to study the impact of the uncertainties in the assumed intrinsic model. The models are obtained by sampling the fit parameters of the nominal model within their corresponding $\pm 1\sigma$ errors and retrieving the minimum and maximum flux values for different values of energy. These flux points are then refitted using *Naima* to get the corresponding parameters of the $\pm 1\sigma$ models to be used in the analysis in an analogous way as performed with the nominal model.

The analysis described in section 3 is repeated for these $\pm 1\sigma$ models and the corresponding results are used to quantify the overall effect of the intrinsic uncertainties in the final containment bands. Figure 7 shows the relative difference in the derived limits when considering these models with respect to the nominal model and computed as in section 4.1 by using equation 5. No significant change is observed between the results of the

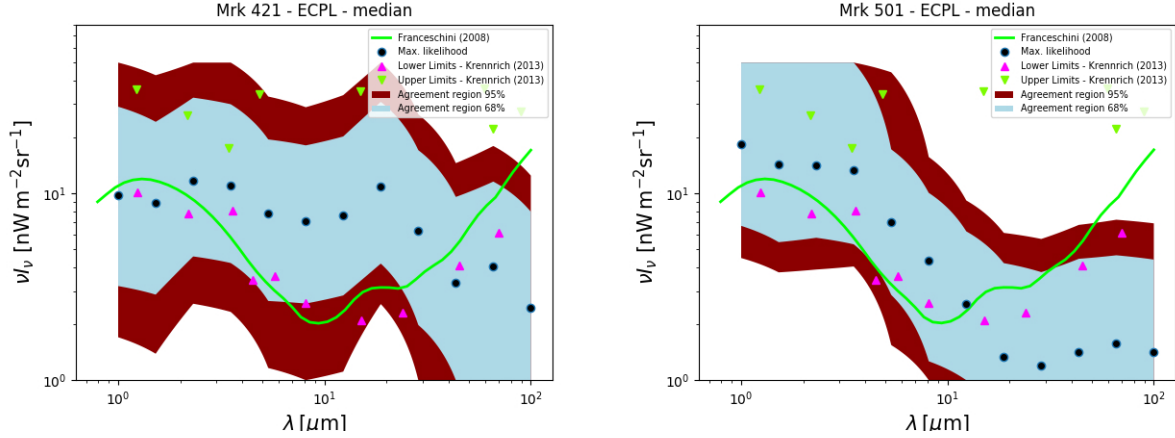


Figure 4. 95% and 68% containment bands for the EBL intensity and different λ values. Red circles correspond to the intensities of the model with the highest likelihood value. Also shown, lower limits from galaxy counts (cyan triangles), upper limits from direct measurements (green triangles) and Franceschini et al. (2008) EBL model for reference.

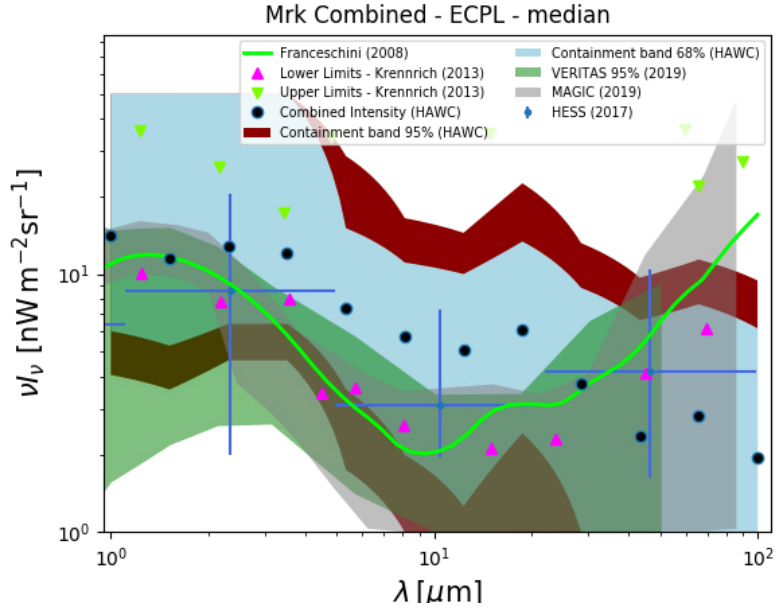


Figure 5. 95% and 68% containment bands for the EBL intensity different λ values for the combined results from Mrk 421 and Mrk 501. Red circles correspond to the combined intensities from each source highest likelihood models (see section 3.3). Also shown, lower limits from galaxy counts (cyan triangles), upper limits from direct measurements (green triangles) and EBL measurements from VERITAS (Abeysekara & Archer 2019), MAGIC (Acciari & Ansoldi 2019) and HESS (Abdalla et al. 2017).

nominal model and the ones resulting from assuming the $\pm 1\sigma$ models, suggesting that the intrinsic spectral assumption gives consistent results within the 1σ uncertainty band.

5. CONCLUSIONS

After years of operation, the HAWC observatory is able to significantly detect extragalactic sources, like the Markarians, up to energies of around 10 TeV. This motivates an analysis that could, in principle, probe the

mid-IR region of the EBL, a region that is inaccessible to other gamma-ray instruments. In this study, physically motivated emission models and *Fermi-LAT* data are used to construct an intrinsic spectrum for each of the Markarians, using the *Naima* python package. A large number of EBL model shapes are randomly generated and used to obtain “observed” spectra to compare with HAWC data of the Markarians. The comparison is performed using *threeML*, in a way that each EBL model can be assigned a likelihood value that ex-

Table 2. Mrk 421 and Mrk 501 combined 68% and 95% credible limits for different λ values. Note: dash indicates that a limit could not be established.

| λ μm | νI_{min} (68% CL) $\text{nW m}^{-2} \text{sr}^{-1}$ | νI_{max} (68% CL) $\text{nW m}^{-2} \text{sr}^{-1}$ | νI_{min} (95% CL) $\text{nW m}^{-2} \text{sr}^{-1}$ | νI_{max} (95% CL) $\text{nW m}^{-2} \text{sr}^{-1}$ |
|----------------------------|---|---|---|---|
| 1.0 | 6.68 | - | 4.49 | - |
| 1.52 | 5.64 | - | 4.01 | - |
| 2.31 | 6.68 | - | 4.76 | - |
| 3.51 | 6.31 | - | 4.49 | - |
| 5.34 | 3.79 | 15.48 | 2.28 | - |
| 8.11 | 2.28 | 10.76 | - | 15.41 |
| 12.33 | 1.71 | 9.79 | - | 14.02 |
| 18.74 | 2.7 | 12.74 | - | 19.91 |
| 28.48 | - | 8.36 | - | 11.87 |
| 43.29 | - | 6.2 | - | 8.73 |
| 65.79 | - | 7.24 | - | 10.46 |
| 100.0 | - | 5.59 | - | 8.2 |

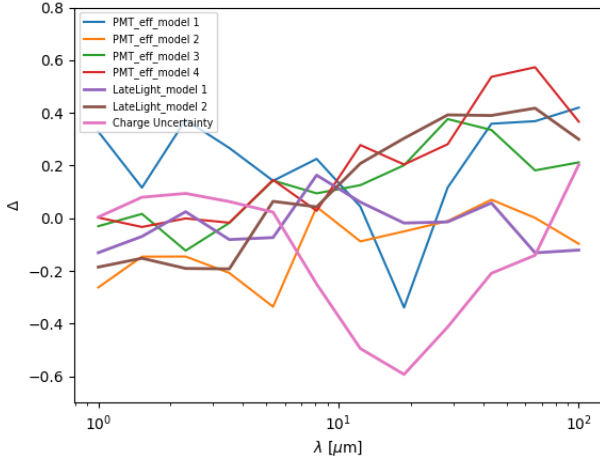


Figure 6. Relative difference between the results considering extreme systematics and the nominal results for different values of wavelength (λ). The meaning of Δ is given by equation 5.

presses the agreement between that particular spectral realization and HAWC data. The present method has the advantage of being independent of any particular EBL shape and assuming physically motivated emission models as intrinsic spectra. The EBL intensity measurements and containment bands are calculated from $1\mu\text{m}$ to $100\mu\text{m}$, probing higher wavelength values than previous measurements performed with VERITAS by using a similar method (Abeysekara & Archer 2019). Results for both sources are in agreement with current upper limits from direct IR observations and lower limits from galaxy counts. Limits are, in general, less constraining for wavelengths below $\lambda \sim 5\mu\text{m}$ and there is a downward trend when moving to higher λ values, roughly follow-

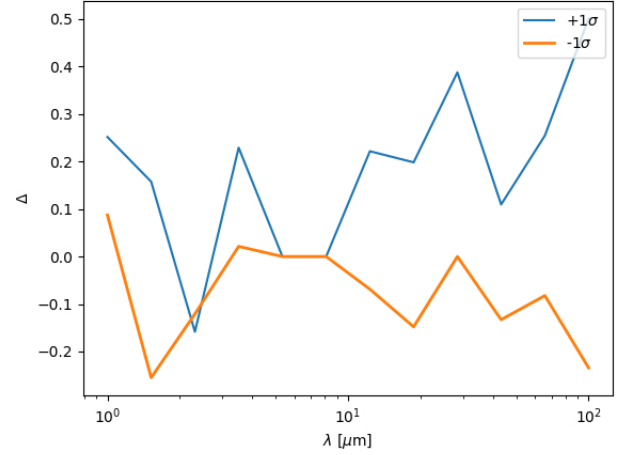


Figure 7. Relative difference between $\pm\sigma$ models and nominal model, for different wavelengths (λ). The meaning of Δ is given by equation 5.

ing the lower limits. This trend is clearer in the case of Mrk 501. A bump around $20\mu\text{m}$ is observed for Mrk 421, possibly due to an observed cutoff drop present in the source observed spectrum around $\sim 5 \text{ TeV}$ Albert et al. (2021a). Results are also in agreement with other instruments EBL intensity estimations reported by HESS (Abdalla et al. 2017) and MAGIC (Acciari & Ansoldi 2019).

These results would surely improve their constraining power if more adequate sources were included. HAWC keeps collecting data from extragalactic sources that could soon be used to derive EBL limits by applying the present method. The radio galaxy M87 was pointed out by Franceschini et al. (2019) as a good candidate to perform EBL related studies. At the time of writ-

ing, this source was detected at too low significance to be reliable for the analysis, therefore it is not included. However, M87 data are being accumulated (Albert et al. 2021b) and will soon provide a significant detection that will make the source useful for this type of analysis.

ACKNOWLEDGMENTS

We acknowledge the support from: the US National Science Foundation (NSF); the US Department of Energy Office of High-Energy Physics; the Laboratory Directed Research and Development (LDRD) program of Los Alamos National Laboratory; Consejo Nacional de Ciencia y Tecnología (CONACyT), México, grants 271051, 232656, 260378, 179588, 254964, 258865, 243290, 132197, A1-S-46288, A1-S-22784, cátedras 873, 1563, 341, 323, Red HAWC, México; DGAPA-UNAM grants IG101320, IN111716-3, IN111419, IA102019, IN110621, IN110521; VIEP-BUAP; PIFI 2012, 2013, PROFOCIE 2014, 2015; the

University of Wisconsin Alumni Research Foundation; the Institute of Geophysics, Planetary Physics, and Signatures at Los Alamos National Laboratory; Polish Science Centre grant, DEC-2017/27/B/ST9/02272; Coordinación de la Investigación Científica de la Universidad Michoacana; Royal Society - Newton Advanced Fellowship 180385; Generalitat Valenciana, grant CIDEAGENT/2018/034; Chulalongkorn University's CUniverse (CUAASC) grant; Coordinación General Académica e Innovación (CGAI-UdeG), PRODEP-SEP UDG-CA-499; Institute of Cosmic Ray Research (ICRR), University of Tokyo, H.F. acknowledges support by NASA under award number 80GSFC21M0002. We also acknowledge the significant contributions over many years of Stefan Westerhoff, Gaurang Yodh and Arnulfo Zepeda Dominguez, all deceased members of the HAWC collaboration. Thanks to Scott Delay, Luciano Díaz and Eduardo Murrieta for technical support.

REFERENCES

- Abdalla, H., Abdalla, H., Abramowski, A., & Aharonian, F. 2017, *A&A*, 606, A59, doi: [10.1051/0004-6361/201731200](https://doi.org/10.1051/0004-6361/201731200)
- Abdo, A. A., & Ackermann, M. 2011, *The Astrophysical Journal*, 727, 129, doi: [10.1088/0004-637x/727/2/129](https://doi.org/10.1088/0004-637x/727/2/129)
- Abdo, A. A., Ackermann, M., Ajello, M., Baldini, L., & Ballet, J. 2011, *The Astrophysical Journal*, 736, 131, doi: [10.1088/0004-637x/736/2/131](https://doi.org/10.1088/0004-637x/736/2/131)
- Abdo, A. A., Ackermann, M., Agudo, I., et al. 2010, *ApJ*, 716, 30, doi: [10.1088/0004-637X/716/1/30](https://doi.org/10.1088/0004-637X/716/1/30)
- Abeysekara, A. U., & Albert, A. 2017, *The Astrophysical Journal*, 843, 40, doi: [10.3847/1538-4357/aa7556](https://doi.org/10.3847/1538-4357/aa7556)
- Abeysekara, A. U., Albert, A., & Alfaro, R. 2019, *The Astrophysical Journal*, 881, 134, doi: [10.3847/1538-4357/ab2f7d](https://doi.org/10.3847/1538-4357/ab2f7d)
- Abeysekara, A. U., & Archer, A. 2019, *The Astrophysical Journal*, 885, 150, doi: [10.3847/1538-4357/ab4817](https://doi.org/10.3847/1538-4357/ab4817)
- Acciari, V. A., & Ansoldi, S. 2019, *MNRAS*, 486, 4233, doi: [10.1093/mnras/stz943](https://doi.org/10.1093/mnras/stz943)
- Aharonian, F., Akhperjanian, A. G., & de Almeida, U. B. 2007, *Astronomy and Astrophysics*, 475, L9, doi: [10.1051/0004-6361:20078462](https://doi.org/10.1051/0004-6361:20078462)
- Albert, A., Alfaro, R., Alvarez, C., & Camacho, J. R. A. 2021a. <https://arxiv.org/abs/2106.03946>
- Albert, A., Alvarez, C., Camacho, J. R. A., et al. 2021b, *The Astrophysical Journal*, 907, 67, doi: [10.3847/1538-4357/abca9a](https://doi.org/10.3847/1538-4357/abca9a)
- Biteau, J., & Williams, D. A. 2015, *The Astrophysical Journal*, 812, 60, doi: [10.1088/0004-637x/812/1/60](https://doi.org/10.1088/0004-637x/812/1/60)
- Cooray, A. 2016, *Royal Society Open Science*, 3, 150555, doi: [10.1098/rsos.150555](https://doi.org/10.1098/rsos.150555)
- Domínguez, A., Primack, J. R., Rosario, D. J., et al. 2011a, *MNRAS*, 410, 2556, doi: [10.1111/j.1365-2966.2010.17631.x](https://doi.org/10.1111/j.1365-2966.2010.17631.x)
- . 2011b, *MNRAS*, 410, 2556, doi: [10.1111/j.1365-2966.2010.17631.x](https://doi.org/10.1111/j.1365-2966.2010.17631.x)
- Dwek, E., & Krennrich, F. 2013, *Astroparticle Physics*, 43, 112, doi: [10.1016/j.astropartphys.2012.09.003](https://doi.org/10.1016/j.astropartphys.2012.09.003)
- Elbaz, D., Cesarsky, C. J., Chanial, P., et al. 2002, *A&A*, 384, 848, doi: [10.1051/0004-6361:20020106](https://doi.org/10.1051/0004-6361:20020106)
- Fazio, G. G., Ashby, M. L. N., Barmby, P., et al. 2004, *ApJS*, 154, 39, doi: [10.1086/422585](https://doi.org/10.1086/422585)
- Franceschini, A., Foffano, L., Prandini, E., & Tavecchio, F. 2019, *Astronomy & Astrophysics*, 629, A2, doi: [10.1051/0004-6361/201935617](https://doi.org/10.1051/0004-6361/201935617)
- Franceschini, A., Rodighiero, G., & Vaccari, M. 2008, *A&A*, 487, 837, doi: [10.1051/0004-6361:200809691](https://doi.org/10.1051/0004-6361:200809691)
- Furniss, A., Williams, D. A., Danforth, C., et al. 2013, *ApJL*, 768, L31, doi: [10.1088/2041-8205/768/2/L31](https://doi.org/10.1088/2041-8205/768/2/L31)
- Gardner, J. P., Brown, T. M., & Ferguson, H. C. 2000, *ApJL*, 542, L79, doi: [10.1086/312930](https://doi.org/10.1086/312930)
- Gerasimova, N. M., Nikishov, A. I., & Rosenthal, I. L. 1962, *Journal of the Physical Society of Japan Supplement*, 17, 175
- Gilmore, R. C., Somerville, R. S., Primack, J. R., & Domínguez, A. 2012, *MNRAS*, 422, 3189, doi: [10.1111/j.1365-2966.2012.20841.x](https://doi.org/10.1111/j.1365-2966.2012.20841.x)

- Gould, R. J., & Schröder, G. P. 1967, *Phys. Rev.*, 155, 1404, doi: [10.1103/PhysRev.155.1404](https://doi.org/10.1103/PhysRev.155.1404)
- Kalbfleisch, J. G. 1985, *Probability and Statistical Inference*, Vol. 2 (Springer)
- Lagache, G., Puget, J.-L., & Dole, H. 2005, *Annual Review of Astronomy and Astrophysics*, 43, 727–768, doi: [10.1146/annurev.astro.43.072103.150606](https://doi.org/10.1146/annurev.astro.43.072103.150606)
- Madau, P., & Phinney, E. S. 1996, *ApJ*, 456, 124, doi: [10.1086/176633](https://doi.org/10.1086/176633)
- Madau, P., & Pozzetti, L. 2000, *MNRAS*, 312, L9, doi: [10.1046/j.1365-8711.2000.03268.x](https://doi.org/10.1046/j.1365-8711.2000.03268.x)
- Mazin, D., & Raue, M. 2007, *A&A*, 471, 439, doi: [10.1051/0004-6361:20077158](https://doi.org/10.1051/0004-6361:20077158)
- Orr, M. R., Krennrich, F., & Dwek, E. 2011, *ApJ*, 733, 77, doi: [10.1088/0004-637X/733/2/77](https://doi.org/10.1088/0004-637X/733/2/77)
- Papovich, C., Dole, H., & Egami, E. 2004, *ApJS*, 154, 70, doi: [10.1086/422880](https://doi.org/10.1086/422880)
- Vianello, G., Lauer, R., Younk, P., et al. 2015, in *International Cosmic Ray Conference*, Vol. 34, 34th International Cosmic Ray Conference (ICRC2015), 1042
- Younk, P. W., Lauer, R. J., Vianello, G., et al. 2015, in *International Cosmic Ray Conference*, Vol. 34, 34th International Cosmic Ray Conference (ICRC2015), 948
- Younk, P. W., Lauer, R. J., Vianello, G., et al. 2015. <https://arxiv.org/abs/1508.07479>
- Zabalza, V. 2015, *naima*: a Python package for inference of relativistic particle energy distributions from observed nonthermal spectra. <https://arxiv.org/abs/1509.03319>
- Zhu, Q., Yan, D., Zhang, P., et al. 2016, *Monthly Notices of the Royal Astronomical Society*, 463, 4481, doi: [10.1093/mnras/stw2346](https://doi.org/10.1093/mnras/stw2346)